AGU PUBLICATIONS

JGR

Journal of Geophysical Research: Solid Earth

RESEARCH ARTICLE
10.1002/2016JB013656

Key Points:
- Creep rates and locking depths of the Chaman fault are assessed with InSAR time series
- The Chaman fault entails substantial creep of up to 11 mm/yr and shallow locking depths (<500 m)
- The earthquake potential of the southern and central Chaman fault is likely low

Supporting Information:
- Supporting Information S1
- Data Set S1

Correspondence to:
W. D. Barnhart,
william-barnhart-1@uiowa.edu

Citation:
Barnhart, W. D. (2017), Fault creep rates of the Chaman fault (Afghanistan and Pakistan) inferred from InSAR, *J. Geophys. Res. Solid Earth*, *122*, 372–386, doi:10.1002/2016JB013656.

Received 17 OCT 2016
Accepted 13 DEC 2016
Accepted article online 14 DEC 2016
Published online 10 JAN 2017

Fault creep rates of the Chaman fault (Afghanistan and Pakistan) inferred from InSAR

William D. Barnhart[1]

[1]Department of Earth and Environmental Sciences, University of Iowa, Iowa City, Iowa, USA

Abstract The Chaman fault is the major strike-slip structural boundary between the India and Eurasia plates. Despite sinistral slip rates similar to the North America-Pacific plate boundary, no major (>*M*7) earthquakes have been documented along the Chaman fault, indicating that the fault either creeps aseismically or is at a late stage in its seismic cycle. Recent work with remotely sensed interferometric synthetic aperture radar (InSAR) time series documented a heterogeneous distribution of fault creep and interseismic coupling along the entire length of the Chaman fault, including an ~125 km long creeping segment and an ~95 km long locked segment within the region documented in this study. Here I present additional InSAR time series results from the Envisat and ALOS radar missions spanning the southern and central Chaman fault in an effort to constrain the locking depth, dip, and slip direction of the Chaman fault. I find that the fault deviates little from a vertical geometry and accommodates little to no fault-normal displacements. Peak-documented creep rates on the fault are 9–12 mm/yr, accounting for 25–33% of the total motion between India and Eurasia, and locking depths in creeping segments are commonly shallower than 500 m. The magnitude of the 1892 Chaman earthquake is well predicted by the total area of the ~95 km long coupled segment. To a first order, the heterogeneous distribution of aseismic creep combined with consistently shallow locking depths suggests that the southern and central Chaman fault may only produce small to moderate earthquakes (<*M*7).

1. Introduction

Slip velocities of faults provide an indirect indicator of the underlying mechanical characteristics of faults and their potential to host future earthquakes [e.g., *Tse and Rice*, 1986; *Scholz*, 1990, 1998]. Interseismically locked faults are expected to generate earthquakes through rapid coseismic slip (m/s) after a period of elastic strain accrual. Within common crustal seismogenic depths (< ~10–15 km), these faults exhibit little to no stable or conditionally stable sliding (i.e., episodic or continuous fault creep) during the interseismic period, and interseismic coupling is often attributed to the static frictional strength of the fault plane. Conversely, faults that slip stably or conditionally stably within seismogenic depths release accrued elastic strain slowly or prevent elastic strain accrual. These behaviors in turn act to lengthen earthquake recurrence intervals, limit the maximum magnitude of an earthquake on a particular fault segment, or prevent the occurrence of earthquakes altogether. Identifying and quantifying the spatial distribution, rates, and depths of aseismic fault creep thus inform probabilistic seismic hazard analysis, and whether the absence of seismicity in earthquake catalogs reflects missing information, a fault late in its seismic cycle, or mechanical conditions that inhibit coseismic fault slip altogether.

Here I use interferometric synthetic aperture radar (InSAR) time series analysis and elastic dislocation modeling to investigate the characteristics of aseismic fault creep along the central and southern Chaman fault of Pakistan and Afghanistan from 28.2°N to 32°N (Figure 1). This region is adjacent to the devastating 1935 *M*7.5 Quetta earthquake that occurred on the neighboring Ghazaband fault [*Singh and Gupta*, 1980; *Ambraseys and Bilham*, 2003; *Szeliga et al.*, 2009] and spans stretches of the Chaman fault that have historically exhibited few significant earthquakes (Figure 1b). Previous InSAR work identified a heterogeneous distribution of shallow fault creep and interseismic locking along the entire length of the Chaman fault [*Fattahi and Amelung*, 2016], with locked portions of the Chaman fault coinciding with the mapped rupture of the 1892 *M*6.5 Chaman earthquake (Figure 1b) [*Ambraseys and Bilham*, 2003]. *Fattahi and Amelung* [2016] found peak sinistral fault slip rates on the Chaman fault of 8.1 mm/yr using a screw dislocation approximation of a vertical strike-slip fault with pure sinistral slip [*Savage and Burford*, 1973]. This rate is in broad agreement with prior estimates of Chaman fault slip rates from campaign GPS surveys [*Szeliga et al.*, 2012]. In the current work, I

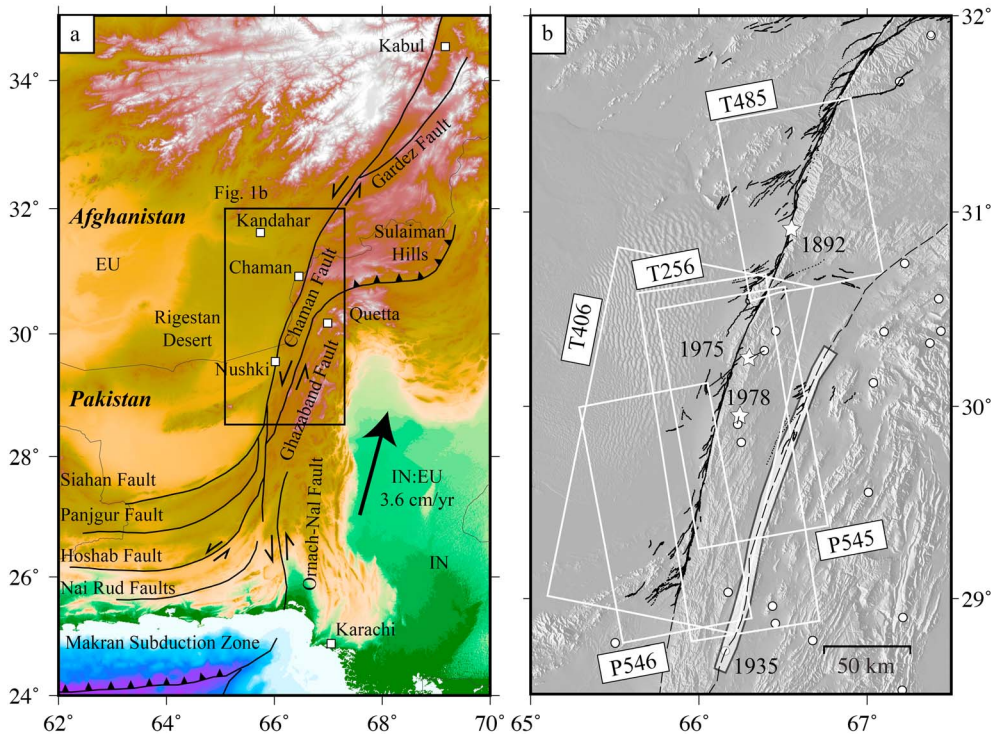

Figure 1. Overview of the Chaman transform boundary and study area. (a) Regional overview of major faults of the Chaman transform boundary (the Chaman, Ghazaband, Ornach-Nal, and Gardez faults) and faults of the Makran accretionary prism [*Lawrence et al.*, 1981; *Ruleman et al.*, 2007]. The vector shows the motion of the India plate relative to Eurasia [*DeMets et al.*, 2010]. Major and regional cities are shown as white squares. Image overlain on the Gebco 2014 DEM [www.gebco.net]. (b) Extent of ALOS (P545 and P546) and Envisat (T256, T485, and T406) imagery (white rectangles) used in this study and regional seismicity. Mapped faults are shown in black [*Ruleman et al.*, 2007]. Approximate locations of other major faults are shown as dashed black lines. Reported locations of significant earthquakes near the Chaman fault and the years that they happened are shown as white stars [*Ambraseys and Bilham*, 2003]. The white dots are instrumentally recorded earthquakes in the ISC GEM catalog [*Storchak et al.*, 2013]. Events present in both catalogs are denoted by the linked lines. The approximate extent of the 1935 Quetta earthquake is shown as the white shaded region [after *Szeliga et al.*, 2012]. Image overlain on the 30 m SRTM DEM [*Farr et al.*, 2007].

build on the analyses of *Fattahi and Amelung* [2016] and *Szeliga et al.* [2012] by exploring the distribution of fault creep rates, variations in geometry and slip direction of the Chaman fault, and changes in locking depth of the Chaman fault as inferred from ascending and descending Envisat and ALOS InSAR time series analysis. I focus on the southern and central portions of the Chaman fault at the northeastern terminus of the Makran accretionary prism. These results are then used to reframe the history of seismicity on and around the Chaman fault and to address the future earthquake potential of this major plate boundary fault.

2. Seismotectonic Background

The Chaman transform boundary of Pakistan and Afghanistan demarks the western boundary of the India plate with the Eurasia plate (Figure 1) [*Lawrence and Yeats*, 1979]. The north-south striking boundary accommodates left-lateral displacements as the India plate moves at ~36 mm/yr relative to the Eurasia plate near 30°N [*DeMets et al.*, 2010]. The southern and central portions of the Chaman transform boundary consist of three major faults: the Chaman fault, the Ghazaband fault, and the Ornach-Nal fault, as well as subsidiary faults (Figure 1a). The continuous surface expression of the Chaman fault originates in the northeastern Makran accretionary prism, near 28.3°N at the juncture of the Siahan and Panjgur faults of the Makran, and extends to ~35°N near Kabul, Afghanistan (Figure 1a) [*Lawrence and Yeats*, 1979; *Lawrence et al.*, 1981]. The Ghazaband fault strikes subparallel to the Chaman fault and originates near 27°N. At ~30.5°N, near Quetta, Pakistan, the Ghazaband transitions to a more eastward strike and merges with thrust faults of the Sulaiman Hills [*Lawrence et al.*, 1981]. The Chaman and Ghazaband faults are offset in a left-lateral sense from

the Ornach-Nal fault, which extends from 27.75°N southward to the Arabian Sea (Figure 1a). Recent observations from the 2013 Baluchistan, Pakistan, strike-slip earthquake on the Hoshab fault (Figure 1a) suggest that this offset originates from counterclockwise block rotations in the southeast Makran which act to reduce left-lateral slip rates on the Ornach-Nal fault [*Barnhart et al.*, 2014; *Jolivet et al.*, 2014]. Geologic field surveys report that the eastern side of the Chaman fault consists of flysch-type sedimentary assemblages that likely originate from the Makran accretionary prism, while the western side of the fault variously comprises of flysch, marine limestones, plutonic granites, and ultramafic intrusions [*Jones*, 1960; *Lawrence and Yeats*, 1979]. Ophiolites and serpentinite bodies have been identified along the active trace of the Chaman fault and other faults throughout the Chaman transform boundary [e.g., *Asrarullah and Abbas*, 1979; *Gansser*, 1979; *Lawrence and Yeats*, 1979; *Tapponnier et al.*, 1981].

Modern geodetic measurements of fault slip rates within the Chaman transform boundary from GPS are sparse but provide important constraints on relative fault motions. *Szeliga et al.* [2012] conducted a campaign GPS survey along a transect that spans the Chaman and Ghazaband faults at 30.5°N–31°N (Figure 2a). Across this transect, they found that the Chaman fault accommodated ~8.5 mm/yr ($\pm$10.3/6.8 mm/yr) of sinistral slip and was likely locked to a depth of 3.4 km. They also found from InSAR observations that the northern Chaman fault (>33°N) likely accommodated velocities of 16.8 $\pm$ 2.7 mm/yr. *Fattahi and Amelung* [2016] built on this work by using Envisat ascending InSAR observations to identify that the Chaman fault creeps aseismically in some locations, alternating between interseimically locked segments and creeping segments along the entire length of the fault. Using a screw dislocation model and the assumptions that the Chaman fault dips vertically, slips with a purely strike-slip sense, and creeps to the surface, they inverted InSAR time series observations to find peak creep rates on the Chaman fault of 8.1 $\pm$ 2 mm/yr. While these modeling assumptions are reasonable given the dearth of geological and geophysical field observations of the Chaman fault, along-strike variations in the dip, locking depth, and slip direction of the Chaman fault may bias creep rates inferred in this manner. The current study seeks to address these potential biases through analysis of the ascending InSAR observations used by *Fattahi and Amelung* [2016] as well as descending InSAR observations that add additional constrains on the three-dimensional surface displacement pattern generated by fault creep.

Seismicity within the Chaman transform boundary and Makran accretionary prism varies substantially among known faults (Figure 2). The largest earthquakes to date in the region include the 2013 M_w7.7 Baluchistan earthquake on the Hoshab fault of the Makran accretionary prism [*Avouac et al.*, 2014; *Barnhart et al.*, 2014; *Jolivet et al.*, 2014] and the 1931 M_w7.2 Mach and 1935 M_w7.5 Quetta earthquakes that occurred on or near the Ghazaband fault (Figures 1 and 2) [e.g., *Singh and Gupta*, 1980; *Ambraseys and Bilham*, 2003; *Szeliga et al.*, 2009]. Unlike the Ghazaband fault, the Ornach-Nal fault has produced no known major or destructive earthquakes larger than an M_w5.9 earthquake in 1974 (U.S. Geological Survey (USGS) Comprehensive Catalog [*Bilham et al.*, 2007]). As described previously, this lack of seismicity may result from a particularly long recurrence interval or the modulation of left-lateral slip rates by counterclockwise rotation of the crustal block west of the Ornach-Nal fault.

Similar to the Ornach-Nal fault, there are few examples of significant earthquakes reliably located on the Chaman fault south of 32°N. An *M*6.5 earthquake in 1892 near the town of Chaman (29.95°N) is well located on the Chaman fault due to records of offset cultural features (Figure 2) [*Griesbach*, 1893; *Ambraseys and Bilham*, 2003]. The location of the 1892 earthquake further coincides with a geodetically imaged locked portion of the Chaman fault [*Szeliga et al.*, 2012; *Fattahi and Amelung*, 2016]. A suite of three earthquakes (M_w5.5, 5.2, and 4.7) occurred near the southern extent of this locked segment on 13 May 2016 (Figure 2b). Two other events of *M*6.8 and *M*6.1 in 1975 and 1978 are also inferred to have ruptured the Chaman fault near 29.8°N (Figure 2). Earthquake location uncertainties for these two events are large though [*Ambraseys and Bilham*, 2003], and there was no evidence of surface rupture on the Chaman fault following the 1978 earthquake [*Yeats et al.*, 1979].

3. Methods

3.1. InSAR Time Series Analysis

To quantify slip rates of the southern and central Chaman fault (29°N–32°N), I used InSAR observations from the European Space Agency Envisat C-band radar and the Japanese Space Agency ALOS-PALSAR L-band

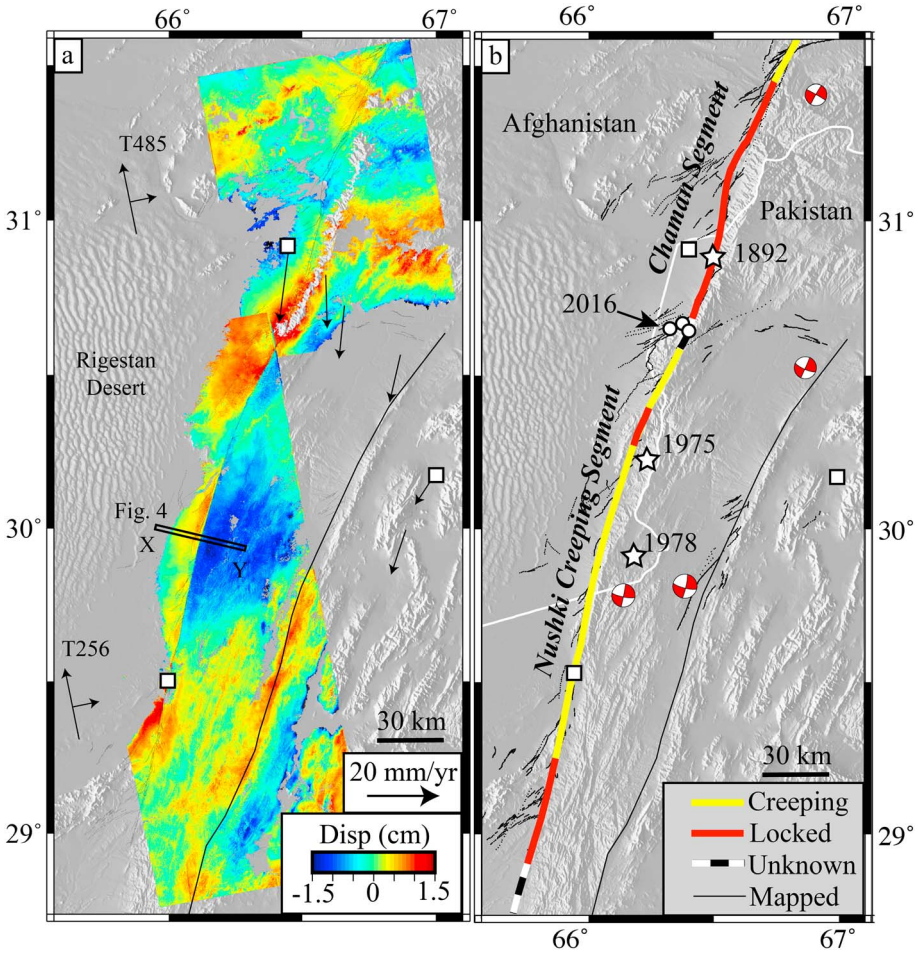

Figure 2. (a) Cumulative line-of-sight (LOS) displacements from ascending Envisat tracks 256 and 485. Positive displacements indicate motion toward the satellite (LOS shortening), and negative displacements indicate motion away from the satellite (LOS lengthening). The double-headed vectors indicate the azimuth and look directions of the satellite in each track. GPS velocities, relative to stable India, are shown as black vectors [*Szeliga et al.*, 2012]. Across-fault displacements from profile X-Y are shown in Figure 4. The interferograms used to generate these displacement maps are illustrated in Figures S1a and S1b. (b) Interpreted map of the Chaman fault denoting the location of creeping and locked segments inferred from InSAR stacks. The white stars indicate the reported locations of historical earthquakes [*Ambraseys and Bilham*, 2003], the white dots highlight the location of the 13 May 2016 earthquakes (USGS Comprehensive Catalog), and focal mechanisms are earthquakes reported in the Global CMT catalog [*Ekström et al.*, 2012]. The white squares in both panels indicate the locations of major cities denoted in Figure 1b; figures are overlain on the shaded SRTM DEM [*Farr et al.*, 2007]. Mapped faults are the same as those in Figure 1b.

radar that span the time range of July 2003 to February 2011 (Figures 1b, 2, and 3). Interferograms were processed from five different viewing geometries that include four ascending and one descending geometries (Figure 1b and Table 1). No observations from the ERS-1/2 satellites are available over this region to allow for an extended observation period. Within each path/track, Envisat interferometric pairs were restricted to perpendicular baselines shorter than 400 m, while no baseline constraint was place on ALOS pairs. I also applied no constraint on temporal baselines (Figure S1 in the supporting information). Individual interferograms were processed with a spatial resolution of 30 m per pixel by using the *InSAR Scientific Computing Environment* [*Agram et al.*, 2013]. Topographic phase was removed with the 30 m Shuttle Radar Topography Mission (SRTM) digital elevation model (DEM) [*Farr et al.*, 2007]. I unwrapped individual filtered interferograms with the *Statistical-cost Network-flow Approach for Phase Unwrapping* [*Chen and Zebker*, 2001]. Interferograms with substantial signal decorrelation were manually culled. I then individually inspected all interferograms for unwrapping errors, as evidenced by large displacement discontinuities between regions of high coherence. Unwrapping errors were manually corrected where the proper phase ambiguity could

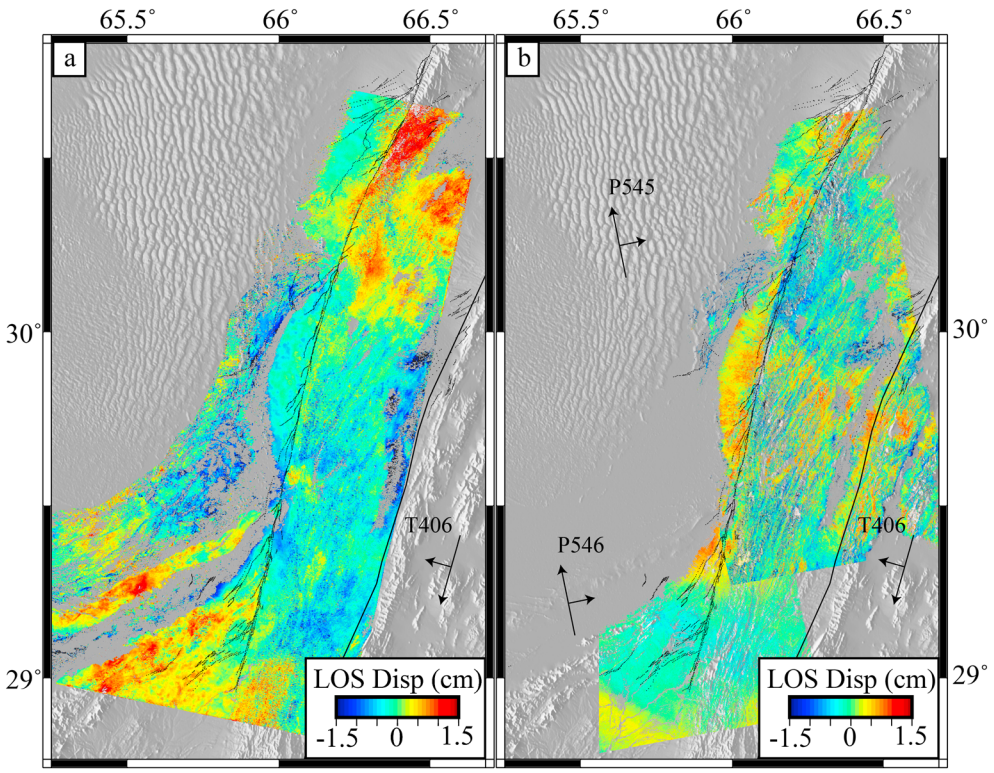

Figure 3. Cumulative surface displacement maps of (a) descending Envisat track 406 and (b) ascending ALOS paths 545 and 546. The arrow designations are the same as in Figure 2a. Mapped faults are the same as those in Figure 1b. The interferograms used to generate these displacement maps are illustrated in Figures S1c–S1e.

be identified, and all other erroneously unwrapped regions were omitted from the analysis. Interferograms were then coregistered to the first interferometric pair within each path/track in the radar coordinate system to form five image stacks.

Each stack of interferograms was then inverted for the line-of-sight (LOS) displacement time series of each pixel by using the Small Baseline Subset algorithm [*Berardino et al.*, 2002] as implemented by the *Generic InSAR Analysis Toolbox* [*Agram et al.*, 2013]. Potential long wavelength phase gradients introduced by orbital errors were removed by using a network deramping approach that iteratively re-estimates orbital ramps by using the entire interferogram stack [e.g., *Biggs et al.*, 2007; *Cavalié et al.*, 2008; *Lin et al.*, 2010]. Given the absence of continuous GPS observations in the study region that may improve confidence in various correction approaches, I did not apply weather-model-based corrections to the interferograms. After inverting for the time series, I extracted and geocoded the cumulative LOS displacement field of each stack and LOS file. In each track, I omitted any pixels that were decorrelated in more than 10% of the available acquisition dates. Lastly, I inverted the time series of each pixel for a linear displacement rate. This rate was then used

Table 1. Details of the InSAR Data Sets Used in This Study[a]

Sensor	Track/Path	Frame	Start	End	Duration (years)	Inc. Angle	No. of Dates
ALOS	545	570, 580	29.12.2006	24.02.2011	4.16	39°	9
ALOS	546	580, 590	27.01.2007	07.02.2011	4.03	39°	18
Envisat	256	567, 585	17.09.2004	01.10.2010	6.04	41°	37
Envisat	406	2997, 3015	01.07.2003	16.03.2010	6.71	22°	32
Envisat	485	603	29.08.2004	01.03.2009	4.50	41°	32

[a]Sensor: satellite used, Track/Path: scene designations given for each interferometric geometry, Frame: the frame numbers used for each track/path, Start: first acquisition date in each stack (format: DD.MM.YYYY), End: last acquisition date in each stack, Duration: total time spanned by each stack, given in years; Inc. Angle: mean incidence angle of the observations, No. of Dates: The number of independent acquisitions used in each stack.

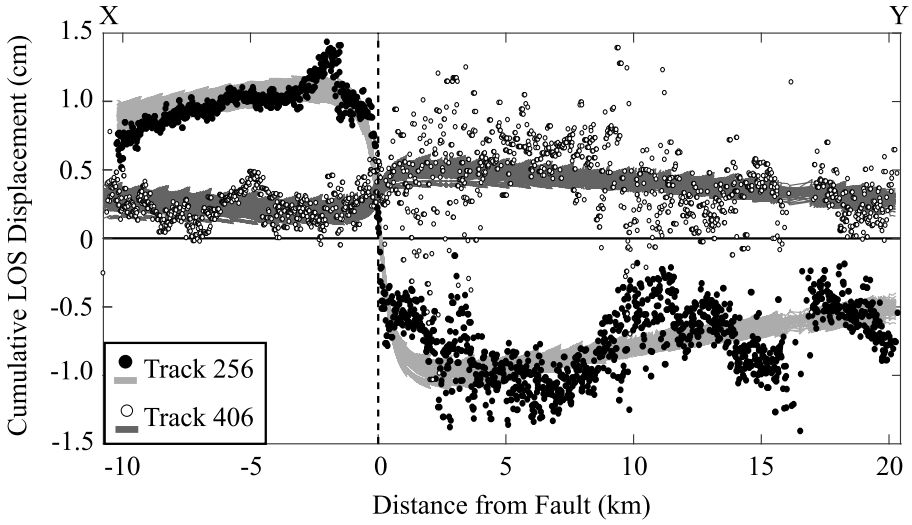

Figure 4. An example of across-fault LOS cumulative displacements from Envisat tracks 256 (block dots) and 406 (white dots) that are used to invert for creep rate, locking depth, fault dip, and slip direction. The dark and light gray profiles illustrate the population of 50 inversion models that are fit to these observations through the detailed Monte Carlo approach. The example shown is for an inversion that inverts both data sets while keeping fault dip and slip direction fixed. The location of profile X-Y is shown in Figure 2a. The profile is plotted with reference to distance from the fault trace of the Chaman fault (distance = 0 km).

to generate an averaged cumulative LOS displacement for each pixel that is used for the creep rate inversions described below (Figures 3 and 4). This step reduces the impact of coherent noise that may dominate a single acquisition date [e.g., *Barnhart and Lohman*, 2013; *Fattahi and Amelung*, 2016].

3.2. Creep Rate Inversions

Numerous studies have implemented a range of inversion strategies to quantify fault slip and creep rates from InSAR, including inverting interferograms directly for subsurface fault slip rate [e.g., *Bürgmann et al.*, 2000; *Johanson and Bürgmann*, 2005; *Schmidt et al.*, 2005; *Jolivet et al.*, 2012] or inverting across-fault displacement profiles to obtain "point" measurements of creep rate [e.g., *Lindsey et al.*, 2014]. In many instances, the magnitude of surface displacements from a strike-slip fault in the radar LOS may be small, either due to slow creep rates or nonideal radar viewing geometries that capture only a limited component of the dominantly horizontal displacements. As a result, inversions for creep rate from InSAR observations alone may be highly nonunique and require substantial regularization, particularly if the subsurface geometry of the creeping fault is not known. In some cases, researchers have applied a horizontal slip constraint on a vertically dipping fault plane (i.e., all displacements are horizontal and fault-parallel) to improve the uniqueness of fault slip inversions [e.g., *Jolivet et al.*, 2012; *Lindsey et al.*, 2014]. *Fattahi and Amelung* [2016] applied this approach in their analysis of Chaman fault creep rates.

Little is known about the geometry of the Chaman fault (i.e., dip) and its principal slip direction. Moreover, the cumulative surface displacement maps span a broad range of time intervals (Table 1), meaning they cannot be jointly inverted for creep rate without introducing a rate bias. To address these issues, I undertake an inversion strategy to constrain a range of creep rates that are compatible with the InSAR time series observations. From visual inspection, fault creep is most apparent in the Envisat track 256 time series spanning the latitude range of 29°N to 30.6°N (Figure 2a). ALOS acquisitions show evidence for fault creep as well (Figure 3b); however, these time series entail significant signal decorrelation, and the displacement time series are noisy, likely due to comparatively fewer acquisition dates (Table 1). As such, my creep rate analysis focuses on the region spanned by Envisat tracks 256 and 406 (Figures 2a and 3a).

To invert for creep rates, I digitized a fault trace from optical imagery, the InSAR time series, and published fault maps [*Ruleman et al.*, 2007] that was then divided into 350 adjoining segments, each of 500 m width. I then extracted the cumulative line-of-sight displacements within a 40 km × 0.5 km swatch perpendicular to each fault segment. For computational efficiency, every tenth pixel was extracted for

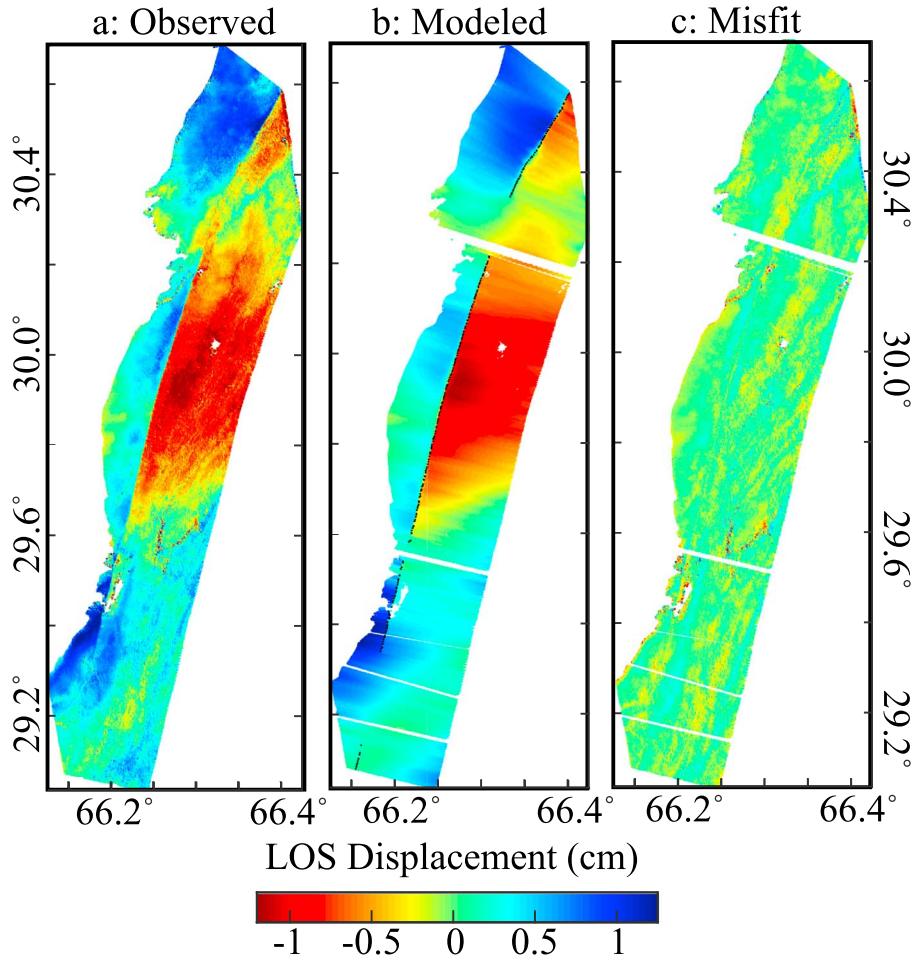

Figure 5. (a) Example of the LOS displacements extracted from profiles crossing the Chaman fault. The example shown is displacements extracted from the Envisat Track 256 time series. (b) LOS displacements predicted by the best fitting creep rate inversion, such as that from Figure 4. Only profiles with inferred velocities slower than 3 cm/yr are shown. The black dots indicate the inverted location of the fault trace for profiles with inferred locking depths shallower than 3 km and plotted in Figures 7 and 9. (c) Misfit between the observed and modeled LOS displacements. This example is from the inversion experiment where dip and rake are held fixed. Similar plots for the other inversion experiments are shown in Figure S2.

the inversion; however, the obliquity of the across-fault profiles to the image grid resulted in an average pixel spacing of 30 m. Many of the profiles do not include displacements extending 20 km fully on either side of the faults, particularly along the western side of the fault (Figures 5 and S2). I first considered only cumulative displacements from track 256, similar to the analysis of *Fattahi and Amelung* [2016] (Figure 2a). For each across-fault profile of surface displacements, I inverted the profile of displacements for the best fitting slip magnitude and locking depth of a dislocation with uniform slip embedded in a homogeneous elastic half-space using the Neighbourhood Algorithm [*Okada*, 1992; *Sambridge*, 1999] (Figure 4). I approximated an infinitely long strike-slip fault by fixing the downdip width and along-strike length of the fault plane to 100 km. The Neighbourhood Algorithm was permitted to search through a range of depths to the top of the fault plane, the value of which is reported as the locking depth of the fault. The best fitting slip magnitude inverted from each profile was then scaled by the duration of the observation period to derive a creep rate. This carries the explicit assumption that creep rates on the Chaman fault are constant over the duration of InSAR observations and that there are no variations in creep rate or coupling ratio downdip of the locking depth. The Neighbourhood Algorithm also inverted the displacements for long-wavelength satellite orbital errors (i.e., ramps) that may still be present in the displacement profiles. This inversion strategy does not account for depth variations in slip rate or the slip rate of the Chaman fault at depths greater than 3–4 km, as is discussed further below.

To test the sensitivity of inferred slip rates to the assumption that the Chaman fault is vertical and displacements are purely fault-parallel [*Fattahi and Amelung*, 2016], I then conducted a suite of inversion experiments with the following constraints:

1. Fault dip = 90°, rake = 0° (left-lateral strike slip);
2. Fault dip = 90°, rake varies from 20 to −20° (left-lateral strike slip with a dip-slip component);
3. Fault dip = 60° to 90° to the east, rake = 0°; and
4. Fault dip = 60° to 90° to the east, rake = 20 to −20°.

The assumption of an eastward dipping fault is based on a suite of test inversions for dip direction and the prevalence of higher relief on the eastern edge of the fault within the study area (Figure 2b). In each iteration, the Neighbourhood Algorithm was permitted to find the best fitting combination of model parameters (depth to the top of the fault plane, slip magnitude, and/or dip and rake). The location and strike of the fault plane were also permitted to vary within a reasonable range (±5° strike, 500 m in a fault-normal direction) to account for local inaccuracies in the mapped fault trace location. The observed, predicted, and residual LOS displacements from each of the inversion experiments are shown in Figures 5 and S2.

Additional to ascending track 256, Envisat descending track 406 provides a different viewing geometry that may reduce the nonuniqueness inherent to inverting a single viewing geometry alone (Figures 1b and 3a). Importantly, track 406 is oriented such that the satellite look direction is approximately perpendicular to the trace of the Chaman fault (Figure 1b). From this geometry, track 406 should be insensitive to fault-parallel displacements (displacements perpendicular to the satellite look direction) and provide an important constraint on where the slip direction is purely strike-slip. Tracks 406 and 256 span different time periods (2450 days versus 2205 days; Table 1), so the cumulative LOS displacements from each cannot be jointly inverted. To address this, I used the LOS linear velocity estimates for each time series, assumed that these velocities are linear over the observation period spanned by both tracks 406 and 256, and then extrapolated the cumulative displacement of each pixel over the time period encompassed by both time series (July 2003 to October 2010, 2649 days). These cumulative displacements were then inverted in the same manner described above (Figure 4).

I constrained the 1-sigma uncertainties of inferred creep rates and locking depths through a Monte Carlo error propagation approach. For each across-fault profile, I subtracted the predicted LOS displacements of the best fitting model from the observed displacements (Figures 5c and S2) and omitted displacements within 1 km of the fault trace to estimate the variance and spatial scale correlation of the displacements in the absence of a deformation source [*Lohman and Simons*, 2005]. I then generated 50 synthetic, noisy data sets by adding spatially correlated noise with the same variance as the displacements to the predicted displacements of the best fitting model. As I have applied no atmospheric corrections, I assume that spatially coherent noise is still present in the time series analysis [*Barnhart and Lohman*, 2013]. Each synthetic data set was then inverted by using the same procedure described above, resulting in 50 populations of model estimates for a single across-fault profile (Figure 4). One-sigma error bounds were defined as the 16th and 84th percentiles of the resulting population of models [e.g., *Devlin et al.*, 2012; *Barnhart et al.*, 2013]. Through this approach, reported error bounds quantify variability introduced by the presence of spatially coherent noise in the InSAR time series. Other potential sources of error, such as deviations from the inference of uniform slip or variations in crustal rigidity structure, are not accounted for in the reported uncertainty ranges.

Lastly, the InSAR time series include substantial signal decorrelation west of the Chaman fault in the sand dunes of the Rigestan Desert (Figures 1–3). Here interferograms that span short time scales (i.e., less than 1 year) are coherent; however, large, short wavelength displacements are apparent, due to drift of the sand dunes, that obscure measurements of stable ground displacements farther than 10–20 km west of the Chaman fault (Figures 2 and 3). Displacements in the Rigestan Desert have been omitted from the time series analysis because of the rarity with which pixels are coherent, but the limited region of coherence west of the Chaman fault and noise in the time series influence the reliable detection of increasingly deep locking depths. To gain a sense of the maximum locking depths that can be detect with the available observations, I conducted a sensitivity test in which I compared the predicted LOS surface displacements of a vertical strike-slip fault accommodating 10 mm/yr of slip to the model residuals of a range of across-fault profiles (Figure 6). I find that locking depths of 3 km or shallower can be reliably detected outside the noise in the InSAR time series. Locking depths greater than 3 km fall within the spread of displacements in model

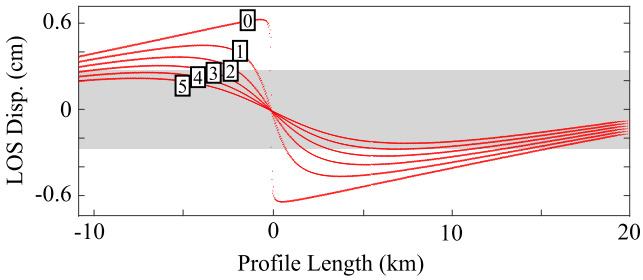

Figure 6. Surface displacement profiles projected into the Envisat ascending track 256 LOS for a vertical strike-slip fault with a 10 mm/yr slip rate. The profiles are denoted by variations in locking depth (km). The gray region represents the spread of residual displacements from a suite of slip rate inversions that is used as a proxy for a deformation detection threshold. Surface displacements that extend outside of this region can be reliably detected, indicating that inferred locking depths of 3 km or shallower can be resolved by the cumulative InSAR displacement fields (Figures 2 and 3).

residuals; thus, I denote profiles where the inferred locking depth is greater than 3 km as interseismically locked (Figure 2b). By extension, slip rates inferred from profiles with locking depths >3 km should be considered unconstrained. Locking depths of 3 km are considerably shallower than the depths typically associated with the width of a seismogenic zone (10–15 km), so a segment denoted in my discussion below as locked should be interpreted as a segment with an unconstrained locking depth greater than 3 km deep.

4. Results

4.1. Extent of Fault Creep

Fault creep is evident in the InSAR time series as a discrete offsets across the Chaman fault (Figures 2–4). In addition to the time series, fault creep is often evident in single interferograms spanning time scales as short as 2 years. Locked segments are inferred for portions of the fault where no discrete offset is evident or where locking depth is unconstrained (>3 km depth) by the available observations (Figure 2). The most prominent creeping feature is the ~150 km long segment of the Chaman fault from ~29.28°N to ~30.58°N (Figure 2a). I term this the "Nushki Creeping Segment" for the town of Nushki transected by the creeping section. The Chaman fault appears locked south of this section, although it may be difficult to detect creep in this region due to the spatial limitations of the InSAR observations, a deeper locking depth, or slower creep rates (i.e., variable coupling ratio along strike). Creep rates decrease substantially within the Nushki Creeping Segment between 30.1°N and 30.4°N before increasing again in the northern portion of the segment. Within an ~15 km stretch of this region, slip rates can only be inferred from inversions where dip is allowed to vary. This restriction may imply that slip rates in this portion of the Nushki Creeping Segment are poorly constrained. The northern terminus of the Nushki Creeping Segment is difficult to precisely identify because of interferometric decorrelation over a 14–15 km length of the fault (Figure 2a); however, InSAR observations suggest that the Chaman fault is locked for an ~95 km long segment of the fault from ~30.7°N to ~31.5°N. The fault then resumes creeping north of 31.5°N, with creep extending beyond the spatial extent of the InSAR observations (Figure 2). The 95 km long locked segment, herein termed the "Chaman Segment" coincides with the GPS transect of *Szeliga et al.* [2012], where they estimated fault slip rates of 8.5 mm/yr and a locking depth of 3.4 km (Figure 2). Coseismic surface ruptures of the 1892 *M*6.5 Chaman earthquake are likewise mapped within this locked segment (Figure 2) [*Ambraseys and Bilham*, 2003]. The locations of earthquakes in 1975 and 1978 estimated to have occurred on the Chaman fault are located adjacent to the Nushki Creeping Segment (Figure 2b).

4.2. Creep Rates

Figure 7 illustrates the distribution of inferred creep rates along the length of the Chaman fault that fall within the observation footprint of Envisat tracks 256 and 406. Inversions from track 256 and track 256/406 show similar patterns of increasing creep rates with increasing latitude within the Nushki Creeping Segment, reaching a peak creep rate of 11 mm/yr (+1/−2 mm/yr) near 29.9°N (Figure 7). Creep rates then progressively decrease to 2 mm/yr (±0.5 mm/yr) in the northern Nushki Creeping Segment before increasing again to 7–9 mm/yr north of 30.4°N. Creep rates are unconstrained from 30.25° to 30.35°N where the locking depth is inferred to be greater than 3 km deep. In inversions of a single look direction (track 256), there is substantial spread in the inferred velocities of the four inversion experiments described previously (Figure 7a). Models that allow slip direction (rake) to vary freely systematically estimate slower slip velocities than inversions where rake is fixed to pure left-lateral slip (0°;

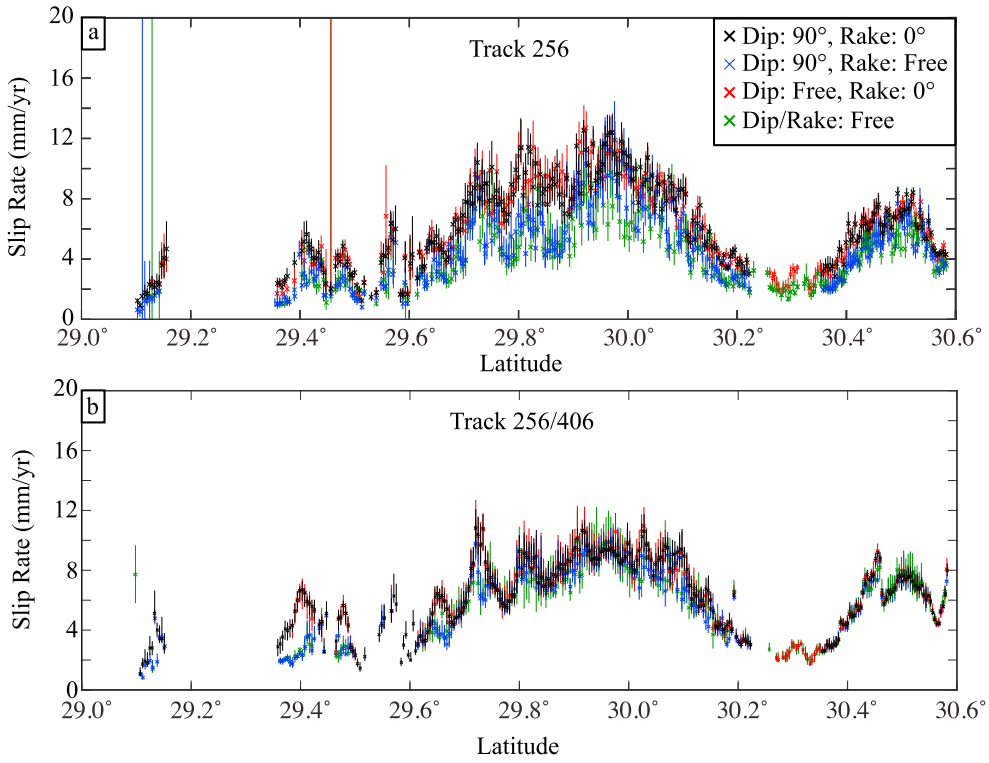

Figure 7. Creep rates of the southern and central Chaman fault (Figure 1b) inferred from Envisat displacements. (a) Creep rates inferred from ascending track 256 alone. The colors represent the results of the different inversion experiments: dip and rake fixed (D90R0; Figure 4), dip fixed and rake free (D90Rf), dip free and rake fixed (DfR0), and dip and rake free (DfRf). (b) Creep rates inferred from both track 256 and descending track 406. The profile designations are the same as in Figure 7a. The vertical bars in both panels are the 1-sigma uncertainties derived from the Monte Carlo analysis (Figure 4). All creep rate values are given in the supporting information.

Figure 7a). In some cases, creep rates inferred from the same across-fault profile vary by nearly a factor of 2 (~6 mm/yr versus ~12 mm/yr) when rake is allowed to vary freely versus fixed to 0°. Unsurprisingly, this spread is greatly reduced in inversions of both available look directions (tracks 256 and 406; Figure 7b). This pattern suggests that the addition of another look angle provides a more robust constraint on rake angle. Within the Nushki Creeping Segment north of ~29.8°N, the four experiments inverted from two look directions agree within uncertainties. Near 29.4°N, inversions that allow rake to vary again find slower creep rates than the fixed rake inversions; however, this discrepancy may be explained by interferometric decorrelation that obscures displacements of $>$5 km west of the fault. (Figure 2a) In other words, the slip rate inversions are likely poorly constrained from 29.3°N to 29.5°N due to the limited spatial coverage of observations.

To investigate the source of potential discrepancies between creep rates evident in Figure 7, Figure 8 compares inferred rake values inferred from single and two look directions. As expected given the slight obliquity of the Chaman fault with respect to the plate motion vector of India (Figure 1), inferred rakes exhibit a slightly oblique-convergent sense. Two general patterns are evident: first, inversions that include observations from two look directions prefer shallower rake angles (0–10°) than inversions of a single look direction (8–14°). Second, inversions that allow both dip and rake angles to vary freely (Figure 8a) exhibit a smaller spread in values than inversions where dip is fixed to 90° (Figure 8b). I interpret these patterns to indicate that (a) rake angles are low and near pure left-lateral slip (0–10°) given the added constraint of a second look direction, as would be expected for any inversion of fault slip direction, and (b) there is an inversion trade-off between dip and rake angles. The relationship between rake and dip angle inverted from single and double look directions is illustrated in Figure S3. Despite these trade-offs, the creep rate profiles in Figure 7 and the inverted values of rake and dip shown in Figures 8 and S3 suggest that (a) creep rates are well and consistently constrained by the inclusion of two look directions despite allowing dip and rake to vary, dip angles deviate little from

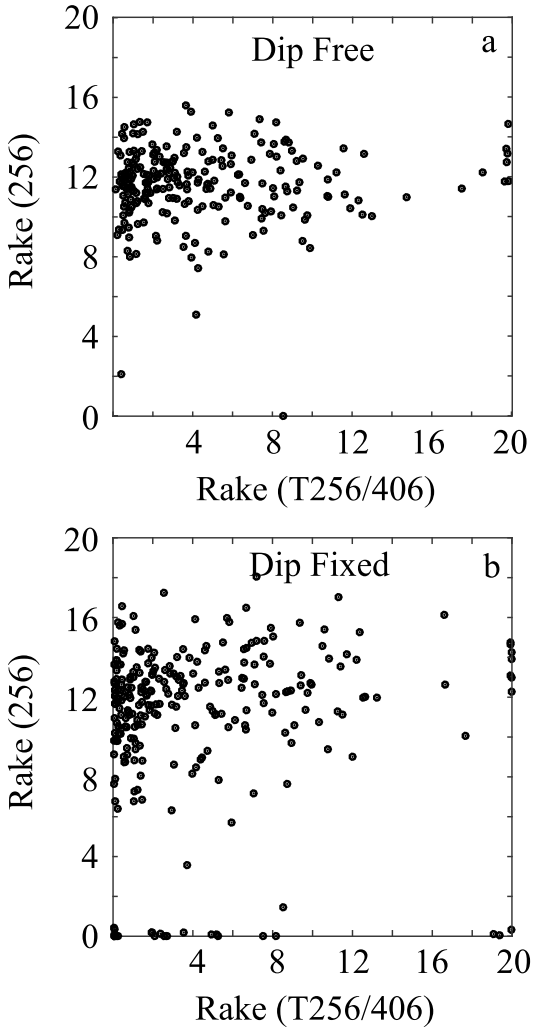

Figure 8. Comparison of inferred slip directions (rake) from inversions where rake was allowed to vary, and inversions that include a single and two look directions. (a) Inversion results where dip is also permitted to vary. (b) Inversion results where dip is fixed to vertical (90°). Comparisons of inverted rake to dip angle are shown in Figure S3. Positive rake angles indicate convergence/reverse-type slip. The reported rake values are the median values derived from the Monte Carlo error analysis.

vertical (87–90°), and rake angles are nearly pure left-lateral (0–10°). These conclusions indicate that the assumption of a pure left-lateral slip on a vertically dipping fault invoked by *Fattahi and Amelung* [2016] likely does not substantially bias their inferred creep rates. These experiments do, however, reinforce the value of multiple interferometric look directions for the purposes of exploring unknown fault geometry and slip direction.

4.3. Locking Depth

The distribution of locking along the Chaman fault is illustrated in Figure 9. Again, inversions for locking from a single look direction (Figure 9a) exhibit greater spread between the four inversion experiments undertaken than inversions from two look directions (Figure 9b). The uncertainty range of locking depths inverted from both look directions is likewise systematically smaller. Locking depths within the Nushki Creeping Segment are routinely shallower than 500 m except from latitudes 30.2°N to 30.5°N where locking depths increase to 500 m–2 km deep (Figure 9b). From an initial inspection, there appears to be a correlation between decreased creep rate (Figure 7) and increased locking depth (Figure 9). However, the mean correlation coefficient between locking depth and creep rate inferred from the four inversion experiments is −0.19, indicating week to negligible anticorrelation between these two parameters. Generally, locking depths that can be reasonably constrained from the available InSAR observations are extraordinarily shallow and consistent with a fault that creeps nearly to the surface.

5. Discussion

The InSAR time series analysis and modeling presented here demonstrates that the southern and central Chaman fault exhibits significant aseismic creep within seismogenic depths shallower than 3 km over a 7.25 year observations period, with the fault commonly locked only to depths of 1 km or shallower (Figures 2, 7, and 9). The rate of creep within creeping segments is heterogeneous along strike, varying in the Nushki Creeping segment from 2 (±1) to 11 (+1/−2) mm/yr (Figure 7). These results are in broad agreement with previous InSAR and GPS studies that found average fault slip rates of ~8 mm/yr [*Szeliga et al.*, 2012; *Fattahi and Amelung*, 2016]. The inversions presented suggest that there may be some variability in both the dip and slip direction of the Chaman fault along strike, yet these variations are small and indicate that the

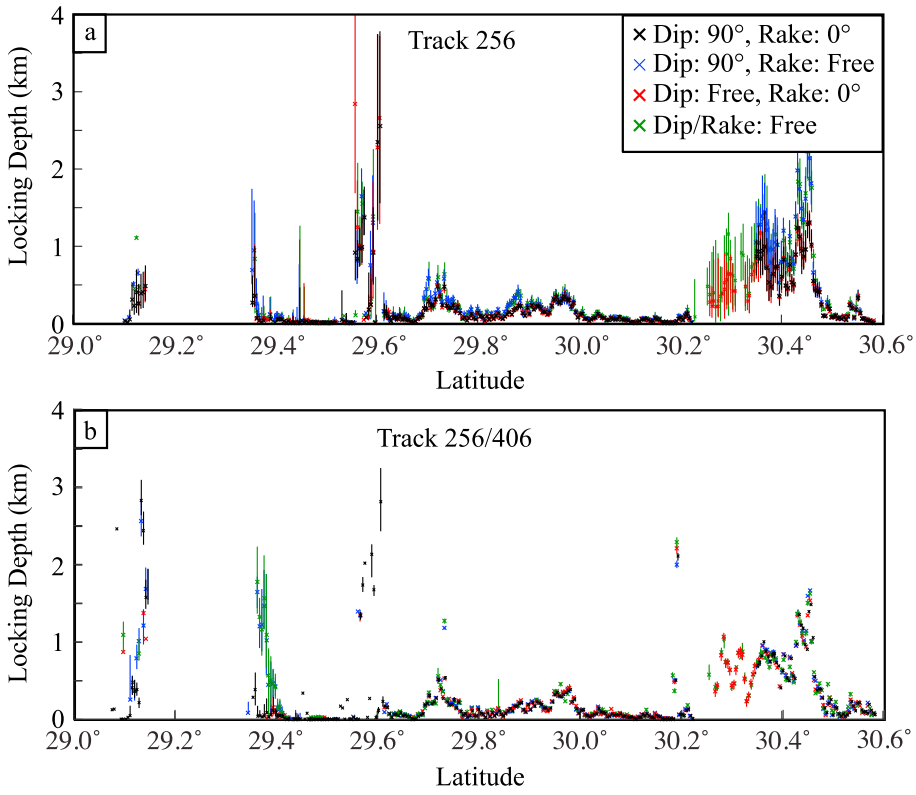

Figure 9. Inferred locking depths of the southern and central Chaman fault. (a) Locking depths inferred from Envisat track 256 only. (b) Locking depths inferred from both track 256 and track 406. The profile designations in both panels are the same as those in Figure 7. The vertical bars indicate the 1-sigma uncertainties derived from the Monte Carlo analysis. All locking depth values are given in the supporting information.

Chaman fault neither dips substantially nor accommodates significant fault-normal displacements within the study area, as is expected from plate motion models (Figures 8 and S3) [e.g., *Jackson et al.*, 1995; *DeMets et al.*, 2010; *Szeliga et al.*, 2012].

The variations in creep rate within the Nushki Creeping Segment highlight an import and as yet unresolved gap in our understanding of strain partitioning within this plate boundary zone (Figure 7). The inferred variations in creep rate may arise from two different sources: variations in the degree of fault coupling on the Chaman fault along strike or partitioning of slip rates onto the neighboring Ghazaband fault and other structures. Because the Chaman fault exhibits both creeping and interseismically locked segments along strike (Figures 2b and 7) [*Szeliga et al.*, 2012; *Fattahi and Amelung*, 2016], it can be inferred that there are along-strike variations in coupling. If it is assumed that the peak measured creep rate of 11 (+1/−2) mm/yr represents the completely uncoupled slip rate of the Chaman fault, then the Chaman fault accommodates 25–33% of the cumulative plate motion between India and Eurasia, and the coupling ratio in the Nushki Creeping Segment varies from 0 to 0.72.

If the Chaman fault indeed accommodates 11 (+1/−2) mm/yr of the 36 mm/yr displacement across the India/Eurasia plate boundary, the remaining 24–27 mm/yr of residual plate motion would then be accommodated on the Ghazaband fault and other structures. *Szeliga et al.* [2012] noted no apparent interseismic accumulation across the northernmost terminus of the Ghazaband fault (adjacent to the Chaman locked segment imaged in this study). Yet large earthquakes have occurred on the Ghazaband fault, so it can be reasonably inferred that slip rates accommodated by the Ghazaband fault vary with latitude. This would potentially act to transfer slip onto or away from the Chaman fault, also causing the slip rate of the Chaman fault to vary with latitude. Thus, it is not clear if the variations in creep rate of the Chaman fault (Figure 7) relate to variations in fault coupling, variations in total slip rate accommodated by the fault, or a combination of both. *Fattahi and Amelung* [2016] estimated the slip rate of the Ghazaband fault to be 16 ± 2 mm/yr at 29°N. When combined

with an estimated 11 mm/yr slip rate on the Chaman fault, these two faults account for 64–83% of the total plate motion across the plate boundary, leaving 6–13 mm/yr of relative plate motion that is accommodated off of these two structures. These estimates are tempered by the fact that there are not currently sufficient observations to determine the degree to which slip is partitioned between the Chaman and Ghazaband faults as a function of latitude. Furthermore, the limited spatial coverage of InSAR observations west of the Chaman fault inhibits the ability to robustly invert for depth variations of creep through a finite fault slip inversion. The inferred maximum slip rate of 11 mm/yr on the Chaman fault would increase if that rate is not representative of the full slip rate of the fault. Further resolving the relative influences of fault coupling and slip partitioning would benefit from additional GPS and InSAR time series observations, as well as estimates of geologic slip rates from multiple locations along these faults in order to better constrain if the short geodetic observation period is representative of long-term slip rates.

Despite these uncertainties, the distribution of creep and locking along the Chaman faults provides a new perspective on the earthquake history of this region (Figure 2b) [*Ambraseys and Bilham*, 2003]. The most notable locked segment in this study area, the Chaman Segment, extends for ~95 km and was the locus of an ~*M*6.5 event in 1892 [*Ambraseys and Bilham*, 2003]. *Szeliga et al.* [2012] found slip rates of 8.5 mm/yr and a locking depth of 3.4 km from a GPS transect spanning the Chaman Segment (Figure 2a). They proposed that the 1892 earthquake would have a recurrence interval of ~100 years with these parameters. Our observations are in very good agreement with this assessment: a 95 km × 3.4 km locked fault accruing a slip deficit of 8.5 mm/yr would produce one *M*6.6 earthquake every 100 years.

The earthquakes in 1975 and 1978 inferred to have ruptured the Chaman fault are not as well explained by the InSAR observations (Figure 2). The location of the *M*6.8 1975 earthquake is in close proximity to the ~17 km long slowly creeping portion of the Nushki creeping segment where locking depths are estimated to be 1–2 km (Figures 2, 7, and 9). A complete rupture of this portion of the creeping segment with a locking depth of 2 km would require 15 m of slip or more, an unlikely scenario given expected earthquake scaling relationships [e.g., *Wells and Coppersmith*, 1994]. It is possible that rupture on this segment or one of the locked segments bounding the Nushki Creeping Segment could propagate some distance into an adjoining creeping segment [e.g., *Noda and Lapusta*, 2013; *Barnhart et al.*, 2016]; however, this earthquake may simply be misattributed to the Chaman fault. Similarly, the 1978 earthquake is located within the latitude range of the fastest creeping portion of the Nushki creeping segment (Figure 2). This earthquake may likewise be misattributed to the Chaman fault or may be mislocated such that it occurred on the Chaman fault south of the Nushki Creeping Segment. In either case, the distinct segmentation of the Chaman fault into creeping and locked segments coupled with the shallow locking depths of the fault suggests that the potential of the Chaman fault to produce large ($>M7$) earthquakes is small.

6. Conclusions

InSAR time series observations reveal a heterogeneous distribution of fault creep and interseismic coupling along the southern and central Chaman fault of Pakistan and Afghanistan. Peak aseismic creep rates of 11 (+1/−2) mm/yr over 7.25 years indicate that the Chaman fault accommodates ~30% of the plate motion between India and Eurasia at the observed latitudes. These creep rate observations are consistent with continuous creep beneath locking depths of a few hundred meters, in agreement with previous studies that explored GPS and InSAR observations over the region [*Szeliga et al.*, 2012; *Fattahi and Amelung*, 2016]. Additionally, I find evidence for two interseismically locked segments of 95 km (the Chaman Segment) and an unknown length (Figure 2b), in agreement with previous studies. A hypothetical, complete rupture of the 95 km long Chaman Segment would produce an earthquake of comparable magnitude to the 1892 *M*6.5 Chaman earthquake, suggesting that this segment may have an ~100 year rupture recurrence interval and is therefore likely late in its seismic cycle. Other earthquakes attributed to the Chaman fault though are inconsistent with the InSAR observations and common assumptions about the slip behavior of creeping fault segments, suggesting that these earthquakes may have occurred on adjacent faults. A thorough analysis of the population of fault parameters (dip, rake, slip rate, and locking depth) that agree with the InSAR observations suggests that the Chaman fault is a near-vertical strike-slip fault that accommodates little to no fault-normal displacements. In particular, this analysis highlights the value of including multiple InSAR look directions to more robustly characterize the geometry and slip direction of a fault.

While I and others are able to identify creeping and locked fault segments along the Chaman fault, the robustness of interpretations drawn from these observations are limited with respect to resolving the distributed fault slip rates of the entire plate boundary zone and the degree of interseismic coupling on the Chaman fault itself. These difficulties arise from two sources. First, the InSAR observations have limited spatial and temporal resolutions, and an ~7 year observation period does not capture potential long-term variations in slip rate of the fault. The sparse temporal sampling of available InSAR observations inhibits the detection of creep events and nonlinear variations in surface displacement rates. The inability to resolve locking depths deeper than 3 km or depth variations in creep rate from the data observations presented here also restricts interpretation of the inferred slip behavior of the Chaman fault throughout the seismogenic zone, particularly in segments inferred to be interseismically locked. Second, current observations cannot fully resolve the degree of slip partitioning within the plate boundary zone between India and Eurasia. This generates potential trade-offs between inferred coupling of the Chaman fault and partitioned slip rates, both of which can explain the variations in creep rates illustrated in Figure 7. Despite these issues, the successful identification of creep and locking with InSAR time series analysis provides a conservative synopsis of fault slip rates in the Chaman fault system. If the reported creep rates are representative of the long-term, interseismic slip behavior of the Chaman fault, these observations suggest that the potential of a large earthquake ($>M7$) on the central and southern Chaman fault is low. Additionally, these observations highlight where future studies may be directed to further elucidate the earthquake potential of the western boundary of the Indian Plate.

Acknowledgments

The author thanks Associate Editor Emma Hill and two anonymous reviewers whose comments greatly improved this manuscript. Envisat imagery was acquired through a European Space Agency Category-1 research proposal agreement; ALOS imagery was acquired through a Japanese Space Agency research proposal agreement; Sentinel-1a imagery was acquired from the Alaska Satellite Facility. Several figures were generated by using the Generic Mapping Tool [*Wessel and Smith*, 1998]. A supporting information is included for this manuscript with three (3) figures and one (1) supplemental data set. This work was supported by NASA Earth Surface and Interior grant NNX16AK81G, NASA New Investigator Program grant NNX16AH53G, and through computational resources provided by the University of Iowa, Iowa City, Iowa. The data used are detailed in Table 1, Figure S1, and section 3.

References

Agram, P. S., R. Jolivet, B. Riel, Y. N. Lin, M. Simons, E. Hetland, M.-P. Doin, and C. Lasserre (2013), New radar interferometric time series analysis toolbox released, *Eos Trans. AGU*, *94*(7), 69–70, doi:10.1002/2013EO070001.

Ambraseys, N., and R. Bilham (2003), Earthquakes and associated deformation in Northern Baluchistan 1892–2001, *Bull. Seismol. Soc. Am.*, *93*(4), 1573–1605, doi:10.1785/0120020038.

Asrarullah, A. Z., and S. G. Abbas (1979), Ophiolites in Pakistan: Introduction, in *Geodynamics of Pakistan*, edited by A. Farah, and K. A. Dejong, pp. 181–192, Geol. Surv. of Pakistan, Quetta, Pakistan.

Avouac, J.-P., F. Ayoub, S. Wei, J.-P. Ampuero, L. Meng, S. Leprince, R. Jolivet, Z. Duputel, and D. Helmberger (2014), The 2013, Mw 7.7 Balochistan earthquake, energetic strike-slip reactivation of a thrust fault, *Earth Planet. Sci. Lett.*, *391*, 128–134, doi:10.1016/j.epsl.2014.01.036.

Barnhart, W. D., and R. B. Lohman (2013), Characterizing and estimating noise in InSAR and InSAR time series with MODIS, *Geochem. Geophys. Geosystems*, *14*, 4121–4132, doi:10.1002/ggge.20258.

Barnhart, W. D., R. B. Lohman, and R. J. Mellors (2013), Active accommodation of plate convergence in Southern Iran: Earthquake locations, triggered aseismic slip, and regional strain rates, *J. Geophys. Res. Solid Earth*, *118*, 5699–5711, doi:10.1002/jgrb.50380.

Barnhart, W. D., G. P. Hayes, R. W. Briggs, R. D. Gold, and R. Bilham (2014), Ball-and-socket tectonic rotation during the 2013 Balochistan earthquake, *Earth Planet. Sci. Lett.*, *403*, 210–216, doi:10.1016/j.epsl.2014.07.001.

Barnhart, W. D., J. R. Murray, R. W. Briggs, F. Gomez, C. P. J. Miles, J. Svarc, S. Riquelme, and B. J. Stressler (2016), Coseismic slip and early afterslip of the 2015 Illapel, Chile, earthquake: Implications for frictional heterogeneity and coastal uplift, *J. Geophys. Res. Solid Earth*, *121*, 6172–6191, doi:10.1002/2016JB013124.

Berardino, P., G. Fornaro, R. Lanari, and E. Sansosti (2002), A new algorithm for surface deformation monitoring based on small baseline differential SAR interferograms, *IEEE Trans. Geosci. Remote Sens.*, *40*(11), 2375–2383, doi:10.1109/TGRS.2002.803792.

Biggs, J., T. Wright, Z. Lu, and B. Parsons (2007), Multi-interferogram method for measuring interseismic deformation: Denali Fault, Alaska, *Geophys. J. Int.*, *170*(3), 1165–1179, doi:10.1111/j.1365-246X.2007.03415.x.

Bilham, R., S. Lodi, S. Hough, S. Bukhary, A. M. Khan, and S. F. A. Rafeeqi (2007), Seismic hazard in Karachi, Pakistan: Uncertain past, uncertain future, *Seismol. Res. Lett.*, *78*(6), 601–613, doi:10.1785/gssrl.78.6.601.

Bürgmann, R., D. Schmidt, R. M. Nadeau, M. d'Alessio, E. Fielding, D. Manaker, T. V. McEvilly, and M. H. Murray (2000), Earthquake potential along the Northern Hayward fault, California, *Science*, *289*(5482), 1178–1182, doi:10.1126/science.289.5482.1178.

Cavalié, O., C. Lasserre, M.-P. Doin, G. Peltzer, J. Sun, X. Xu, and Z.-K. Shen (2008), Measurement of interseismic strain across the Haiyuan fault (Gansu, China), by InSAR, *Earth Planet. Sci. Lett.*, *275*(3–4), 246–257, doi:10.1016/j.epsl.2008.07.057.

Chen, C. W., and H. A. Zebker (2001), Two-dimensional phase unwrapping with use of statistical models for cost functions in nonlinear optimization, *J. Opt. Soc. Am. A Opt. Image Sci. Vis.*, *18*(2), 338–351.

DeMets, C., R. G. Gordon, and D. F. Argus (2010), Geologically current plate motions, *Geophys. J. Int.*, *181*(1), 1–80, doi:10.1111/j.1365-246X.2009.04491.x.

Devlin, S., B. L. Isacks, M. E. Pritchard, W. D. Barnhart, and R. B. Lohman (2012), Depths and focal mechanisms of crustal earthquakes in the central Andes determined from teleseismic waveform analysis and InSAR, *Tectonics*, *31*, TC2002, doi:10.1029/2011TC002914.

Ekström, G., M. Nettles, and A. M. Dziewoński (2012), The global CMT project 2004–2010: Centroid-moment tensors for 13,017 earthquakes, *Phys. Earth Planet. Inter.*, *200–201*, 1–9, doi:10.1016/j.pepi.2012.04.002.

Farr, T. G., et al. (2007), The Shuttle Radar Topography Mission, *Rev. Geophys.*, *45*, RG2004, doi:10.1029/2005RG000183.

Fattahi, H., and F. Amelung (2016), InSAR observations of strain accumulation and fault creep along the Chaman fault system, Pakistan and Afghanistan, *Geophys. Res. Lett.*, *43*, 8399–8406, doi:10.1002/2016GL070121.

Gansser, A. (1979), Reconnaissance visit to the ophiolites in Baluchistan and the Himalaya, in *Geodynamics Pakistan*, pp. 193–213 , Geol. Surv. of Pakistan, Quetta, Pakistan.

Griesbach, C. L. (1893), Notes on the earthquake in Baluchistan on the 20th December 1892, *Rec. Geol. Surv. India*, *26*, 57–64.

Jackson, J., J. Haines, and W. Holt (1995), The accommodation of Arabia-Eurasia Plate convergence in Iran, *J. Geophys. Res.*, *100*, 15,205–15,219, doi:10.1029/95JB01294.

Johanson, I. A., and R. Bürgmann (2005), Creep and quakes on the northern transition zone of the San Andreas fault from GPS and InSAR data, *Geophys. Res. Lett.*, *32*, L14306, doi:10.1029/2005GL023150.

Jolivet, R., C. Lasserre, M.-P. Doin, S. Guillaso, G. Peltzer, R. Dailu, J. Sun, Z.-K. Shen, and X. Xu (2012), Shallow creep on the Haiyuan Fault (Gansu, China) revealed by SAR Interferometry, *J. Geophys. Res.*, *117*, B06401, doi:10.1029/2011JB008732.

Jolivet, R., et al. (2014), The 2013 Mw 7.7 Balochistan Earthquake: Seismic Potential of an Accretionary Wedge, *Bull. Seismol. Soc. Am.*, *104*(2), 1020–1030, doi:10.1785/0120130313.

Jones, A. G. (1960), Reconnaissance geology of part of West Pakistan, A Colombo Plan Co-operative Project, Government of Pakistan, Hunt. Surv. Corp. Rep., 550.

Lawrence, R. D., and R. S. Yeats (1979), Geological reconnaissance of the Chaman fault in Pakistan, in *Geodynamics of Pakistan*, edited by A. Farah and K. A. DeJong, pp. 351–357, Geol. Surv. of Pakistan, Quetta, Pakistan.

Lawrence, R. D., R. S. Yeats, S. H. Khan, A. Farah, and K. A. DeJong (1981), Thrust and strike slip fault interaction along the Chaman transform zone, Pakistan, *Geol. Soc. Lond. Spec. Publ.*, *9*(1), 363–370, doi:10.1144/GSL.SP.1981.009.01.33.

Lin, Y. N., M. Simons, E. A. Hetland, P. Muse, and C. DiCaprio (2010), A multiscale approach to estimating topographically correlated propagation delays in radar interferograms, *Geochem. Geophys. Geosyst.*, *11*, Q09002, doi:10.1029/2010GC003228.

Lindsey, E. O., Y. Fialko, Y. Bock, D. T. Sandwell, and R. Bilham (2014), Localized and distributed creep along the southern San Andreas Fault, *J. Geophys. Res. Solid Earth*, *119*, 7909–7922, doi:10.1002/2014JB011275.

Lohman, R. B., and M. Simons (2005), Some thoughts on the use of InSAR data to constrain models of surface deformation: Noise structure and data downsampling, *Geochem. Geophys. Geosyst.*, *6*, Q01007, doi:10.1029/2004GC000841.

Noda, H., and N. Lapusta (2013), Stable creeping fault segments can become destructive as a result of dynamic weakening, *Nature*, *493*(7433), 518–521, doi:10.1038/nature11703.

Okada, Y. (1992), Internal deformation due to shear and tensile faults in a half-space, *Bull. Seismol. Soc. Am.*, *82*(2), 1018–1040.

Ruleman, C. A., A. J. Crone, M. N. Machette, K. M. Haller, and K. S. Rukstales (2007), Map and database of probably and possible quaternary faults in Afghanistan, USGS Afghanistan Project Product No. 150, USGS Open-File Rep.

Sambridge, M. (1999), Geophysical inversion with a neighbourhood algorithm—I. Searching a parameter space, *Geophys. J. Int.*, *138*(2), 479–494, doi:10.1046/j.1365-246X.1999.00876.x.

Savage, J. C., and R. O. Burford (1973), Geodetic determination of relative plate motion in central California, *J. Geophys. Res.*, *78*, 832–845, doi:10.1029/JB078i005p00832.

Schmidt, D. A., R. Bürgmann, R. M. Nadeau, and M. d'Alessio (2005), Distribution of aseismic slip rate on the Hayward fault inferred from seismic and geodetic data, *J. Geophys. Res.*, *110*, B08406, doi:10.1029/2004JB003397.

Scholz, C. H. (1990), *The Mechanics of Earthquakes and Faulting*, 1st ed., Cambridge Univ. Press, New York.

Scholz, C. H. (1998), Earthquakes and friction laws, *Nature*, *391*(6662), 37–42, doi:10.1038/34097.

Singh, D. D., and H. K. Gupta (1980), Source dynamics of two great earthquakes of the Indian subcontinent: The Bihar-Nepal earthquake of January 15, 1934 and the Quetta earthquake of May 30, 1935, *Bull. Seismol. Soc. Am.*, *70*(3), 757–773.

Storchak, D. A., D. D. Giacomo, I. Bondár, E. R. Engdahl, J. Harris, W. H. K. Lee, A. Villaseñor, and P. Bormann (2013), Public release of the ISC–GEM global instrumental earthquake catalogue (1900–2009), *Seismol. Res. Lett.*, *84*(5), 810–815, doi:10.1785/0220130034.

Szeliga, W., R. Bilham, D. Schelling, D. M. Kakar, and S. Lodi (2009), Fold and thrust partitioning in a contracting fold belt: Insights from the 1931 Mach earthquake in Baluchistan, *Tectonics*, *28*, TC5019, doi:10.1029/2008TC002265.

Szeliga, W., R. Bilham, D. M. Kakar, and S. H. Lodi (2012), Interseismic strain accumulation along the western boundary of the Indian subcontinent, *J. Geophys. Res.*, *117*, B08404, doi:10.1029/2011JB008822.

Tapponnier, P., M. Mattauer, F. Proust, and C. Cassaigneau (1981), Mesozoic ophiolites, sutures, and arge-scale tectonic movements in Afghanistan, *Earth Planet. Sci. Lett.*, *52*(2), 355–371, doi:10.1016/0012-821X(81)90189-8.

Tse, S. T., and J. R. Rice (1986), Crustal earthquake instability in relation to the depth variation of frictional slip properties, *J. Geophys. Res.*, *91*, 9452–9472, doi:10.1029/JB091iB09p09452.

Wells, D. L., and K. J. Coppersmith (1994), New empirical relationships among magnitude, rupture length, rupture width, rupture area, and surface displacement, *Bull. Seismol. Soc. Am.*, *84*(4), 974–1002.

Wessel, P., and W. H. F. Smith (1998), New, improved version of generic mapping tools released, *Eos Trans. AGU*, *79*(47), 579–579, doi:10.1029/98EO00426.

Yeats, R. S., R. D. Lawrence, S. Jamil-Ud-Din, and S. H. Khan (1979), Surface effects of the 16 March 1978 earthquake, Pakistan-Afghanistan border, in *Geodynamics Pakistan*, pp. 359–361, Geol. Surv. Pakistan, Quetta, Pakistan.